A&A 643, A95 (2020)
https://doi.org/10.1051/0004-6361/202039195

Astronomy & Astrophysics

R-matrix electron-impact excitation data for the N-like iso-electronic sequence

Junjie Mao[1], N. R. Badnell[1], and G. Del Zanna[2]

[1] Department of Physics, University of Strathclyde, Glasgow G4 0NG, UK
e-mail: junjie.mao@strath.ac.uk
[2] Department of Applied Mathematics and Theoretical Physics, University of Cambridge, Cambridge CB3 0WA, UK

Received 17 August 2020 / Accepted 20 September 2020

ABSTRACT

Context. Spectral lines from N-like ions can be used to measure the temperature and density of various types of astrophysical plasmas. The atomic databases of astrophysical plasma modelling codes still have room for improvement in their electron-impact excitation data sets for N-like ions, especially for *R*-matrix data. This is particularly relevant for future observatories (e.g. Arcus), which will host high-resolution spectrometers.
Aims. We aim to obtain level-resolved effective collision strengths for all transitions up to nl = 5d over a wide range of temperatures for N-like ions from O II to Zn XXIV (i.e. O^+ to Zn^{23+}) and to assess the accuracy of the present work. We also examine the impact of our new data on plasma diagnostics by modelling solar observations with CHIANTI.
Methods. We carried out systematic *R*-matrix calculations for N-like ions, which included 725 fine-structure target levels in both the configuration interaction target and close-coupling collision expansions. The *R*-matrix intermediate coupling frame transformation method was used to calculate the collision strengths, while the AUTOSTRUCTURE code was used for the atomic structures.
Results. We compare the present results for selected ions with those in archival databases and the literature. The comparison covers energy levels, oscillator strengths, and effective collision strengths. We show examples of improved plasma diagnostics when compared to CHIANTI models, which use only distorted wave data as well as some using previous *R*-matrix data. The electron-impact excitation data are archived according to the Atomic Data and Analysis Structure (ADAS) data class *adf04* and will be available in OPEN-ADAS. The data can be used to improve the atomic databases for astrophysical plasma diagnostics.

Key words. atomic data – techniques: spectroscopic – Sun: corona

1. Introduction

Plasma codes widely used in astronomy (e.g. AtomDB[1], CHIANTI[2], SPEX[3]) aim to have extensive and accurate atomic data for a wide range of ions and processes in order to enable the spectroscopic diagnosis of various types of astrophysical plasmas, including, for instance, the outer solar atmosphere (e.g. Del Zanna & Mason 2018), planetary nebulae (e.g. Osterbrock & Ferland 2006), and ionised outflows in active galactic nuclei (Mao et al. 2017). Nevertheless, the latest atomic databases used by astrophysical plasma codes are still not as complete and accurate as we would wish. Improvements in both completeness and accuracy are essential, especially for the next generation of spectrometers to be found aboard future observatories, such as Arcus (Smith et al. 2016), ATHENA/X-ray Integral Field Unit (Barret et al. 2018), and Hot Universe Baryon Surveyor (Cui et al. 2020).

Electron-impact excitation is one of the dominant atomic processes populating excited levels (including the metastable levels), which subsequently leads to emission lines from excited levels to the ground and metastable levels, as well as absorption lines from excited levels. Thus, the precision of plasma diagnostics relies on the accuracy of the electron-impact excitation data.

In terms of *R*-matrix electron-impact excitation data, systematic calculations for many iso-electronic sequences (Li-, Be-, B-, F-, Ne-, Na-, and Mg-like) have been performed over the past decade (see Badnell et al. 2016 for a review, and Mao et al. 2020 for the most recent C-like one). When *R*-matrix data are not available, then either interpolated data, from adjacent ions in the same iso-electronic sequence, or less accurate distorted wave data are used, if available.

Most of the existing *R*-matrix calculations have been performed for individual N-like ions. The number of energy levels of the target ion and the temperature range of the effective collision strength vary significantly. For instance, Tayal (2007) provided effective collision strengths for O II between 47 energy levels over a temperature range of $10^{3.3-5}$ K. Ramsbottom & Bell (1997) obtained effective collision strengths for Mg VI between 23 energy levels over a temperature range of $10^{5.0-6.1}$ K. Liang et al. (2011) provided effective collision strengths for S X between 84 energy levels over a temperature range of $10^{4.3-8.3}$ K. Witthoeft et al. (2007) calculated effective collision strengths for Fe XX between 302 energy levels over a temperature range of $10^{2.0-8.3}$ K.

On the other hand, Wang et al. (2018) presented a systematic *R*-matrix calculation for N-like ions, from Na V to Ca XIV. We note that 272 energy levels were included for each target ion. Effective collision strengths for transitions from the ground level are available over the temperature range $10^{4.0-7.0}$ K .

Atomic data with a larger number of energy levels would be preferred by observers. With advances in technology, we are

[1] http://www.atomdb.org/Webguide/webguide.php
[2] https://www.chiantidatabase.org/
[3] https://www.sron.nl/astrophysics-spex

Table 1. Configurations used for the structure and collision calculations.

Index	Conf.	Index	Conf.	Index	Conf.
1	$2s^22p^3$	2	$2s2p^4$	3	$2p^5$
4	$2s^22p^23s$	5	$2s^22p^23p$	6	$2s^22p^23d$
7	$2s2p^33s$	8	$2s2p^33p$	9	$2s2p^33d$
10	$2p^43s$	11	$2p^43p$	12	$2p^43d$
13	$2s^22p^24s$	14	$2s^22p^24p$	15	$2s^22p^24d$
16	$2s^22p^24f$	17	$2s2p^34s$	18	$2s2p^34p$
19	$2s2p^34d$	20	$2s2p^34f$	21	$2p^44s$
22	$2p^44p$	23	$2p^44d$	24	$2p^44f$
25	$2s^22p^25s$	26	$2s^22p^25p$	27	$2s^22p^25d$

able to observe more and more transitions, which can be used for plasma diagnostics. A wide temperature range would also be favoured by observers probing astrophysical plasmas, ranging from the near-infrared band to the X-ray band. This includes collisional ionised plasmas (up to several million degrees Kelvin) in groups and clusters of galaxies, photoionised plasmas exposed to stars or active galactic nuclei, charge exchange plasma in the interface between the hot and cold gas, and non-equilibrium ionisation plasmas often observed in supernova remnants.

Following systematic intermediate coupling frame transformation (ICFT) *R*-matrix calculations for C-like ions (Mao et al. 2020), here we present similar calculations for N-like ions from N II to Zn XXIV (i.e. N^+ to Zn^{23+}). For each ion, we obtain effective collision strengths between 725 levels over a temperature range spanning five orders of magnitude.

We describe the structure and collision calculations in Sects. 2.1 and 2.2, respectively. Results and discussions are provided in Sects. 3 and 4, respectively. A summary is provided in Sect. 5. In addition, we provide a supplementary package at Zenodo (Mao 2020). This package includes the input files of the structure and collision calculations, atomic data from the present work, archival databases and literature. This package also includes scripts used to create the figures presented in this paper.

2. Method

We adopted the same approach for the structure and collision calculations, described in Sects. 2.1 and 2.2, as detailed in Mao et al. (2020) for C-like ions. The main difference for N-like ions is that we included a total of 725 fine-structure levels in both the configuration-interaction target expansion and the close-coupling collision expansion. These levels arise from the 27 configurations listed in Table 1.

2.1. Structure

We used AUTOSTRUCTURE (Badnell 2011) to calculate the target atomic structure. The wave functions are calculated via diagonalising the Breit-Pauli Hamiltonian (Eissner et al. 1974). The one-body relativistic terms: mass-velocity, nuclear plus Blume & Watson spin-orbit and Darwin, are included perturbatively. We use the Thomas-Fermi-Dirac-Amaldi model for the electronic potential. The *nl*-dependent scaling parameters (Nussbaumer & Storey 1978) are obtained following the procedure presented in Mao et al. (2020) without manual re-adjustment. This ensures that we do not introduce arbitrary changes across the iso-electronic sequence. We list the scaling parameters for the 13 atomic orbitals from 1s to 5d in Table 2. These scaling parameters are used for both the structure and collision calculations for all the ions ($Z = 8-30$) in the sequence.

As shown later in Sect. 4, the atomic structure obtained in the present work shows relatively large deviations with respect to experiment for low-charge ions (e.g. O II, Mg VI) and low-lying energy levels. This is because we use a unique set of non-relativistic orthogonal orbitals (Berrington et al. 1995) – this is required by the ICFT *R*-matrix method, the calculations with which are described next (Sect. 2.2).

The Dirac *R*-matrix method (DARC) and associated multi-configuration Dirac-Fock (MCDF) structure use a unique set of orthogonal orbitals. The B-spline *R*-matrix method (BSR) and associated multi-configuration Hartree-Fock (MCHF) structure can use non-unique and/or non-orthogonl orbitals. These approaches are more computationally expensive for the scattering calculations, especially the BSR method. Del Zanna et al. (2019) performed a detailed case study for N IV where they generated line intensities from three different available atomic data sets (AUTOSTRUCTURE + ICFT, MCHF + BSR, MCDF + DARC) which used the same set of target states. They found agreement between all of the spectroscopically relevant line intensities (within 20%), which provides confidence in the reliability of the present calculations for plasma diagnostics.

2.2. Collision

The ICFT *R*-matrix collision calculation consists of an energy-independent inner-region and energy-dependent outer-region calculation (Burke 2011) for each ion. For both, we included angular momenta up to $2J = 22$ and $2J = 76$ for the exchange and non-exchange, respectively, calculations. For higher angular momenta, up to infinity, we used the top-up formula of the Burgess sum rule (Burgess 1974) for dipole allowed transitions and a geometric series for the non-dipole allowed transitions (Badnell & Griffin 2001).

The energy-dependent outer-region *R*-matrix calculation consists of three separate calculations, for each ion. Firstly, an exchange calculation using a fine energy mesh between the first and last thresholds to sample the resonances. Along the iso-electronic sequence, the number of sampling points in the fine energy mesh was increased with atomic number, ranging from ~3600 for O II to ~30 000 for Zn XXIV, to strike the balance between the computational cost and resonance sampling. Secondly, an exchange calculation using a coarse energy mesh from the last threshold up to three times the ionisation potential. We used ~1000 points for all the ions in the iso-electronic sequence for this coarse energy mesh. Thirdly, a non-exchange calculation using another coarse energy mesh, this time from the first threshold up to three times the ionisation potential. We used ~1400 energy points for all ions in the iso-electronic sequence. Since this coarse energy mesh covers the resonance region, post-processing is necessary to remove any unresolved resonances in the ordinary collision strengths.

The effective collision strength (Υ_{ij}) for electron-impact excitation is obtained by convolving the ordinary collision strength (Ω_{ij}) with the Maxwellian energy distribution:

$$\Upsilon_{ij} = \int \Omega_{ij} \exp\left(-\frac{E}{kT}\right) \mathrm{d}\left(\frac{E}{kT}\right), \quad (1)$$

where E is the kinetic energy of the scattered free electron, k the Boltzmann constant, and T the electron temperature of the plasma. Ordinary collision strengths at high collision energies

Table 2. Thomas-Fermi-Dirac-Amaldi potential scaling parameters used in the AUTOSTRUCTURE calculations for the N-like iso-electronic sequence. Z is the atomic number, e.g. 14 for silicon.

Z	1s	2s	2p	3s	3p	3d	4s	4p	4d	4f	5s	5p	5d
8	1.47243	1.19629	1.13955	1.20168	1.16406	1.17932	1.18660	1.14257	1.15107	1.16400	1.18518	1.13943	1.15198
9	1.45362	1.17931	1.12446	1.22623	1.13000	1.22212	1.20449	1.18226	1.21296	1.26254	1.21160	1.13470	1.23432
10	1.44249	1.18077	1.12217	1.23875	1.19102	1.23133	1.22180	1.14969	1.23266	1.33308	1.20665	1.15497	1.20116
11	1.43358	1.18277	1.12101	1.23576	1.18272	1.25018	1.23599	1.15849	1.22453	1.42000	1.20838	1.17514	1.21844
12	1.42605	1.18458	1.12034	1.24622	1.19278	1.24875	1.22033	1.17594	1.23092	1.35497	1.21371	1.16930	1.22455
13	1.41966	1.18610	1.11999	1.24145	1.19028	1.25897	1.21910	1.17880	1.23582	1.29772	1.21143	1.16123	1.24206
14	1.41417	1.18747	1.11982	1.24435	1.18700	1.24794	1.22099	1.16679	1.24421	1.31233	1.22326	1.16993	1.22339
15	1.40948	1.18866	1.11978	1.24183	1.18889	1.25273	1.21969	1.17337	1.24281	1.17666	1.23428	1.16560	1.23656
16	1.40539	1.18970	1.11982	1.24041	1.18811	1.25768	1.21395	1.16949	1.24177	1.08911	1.24444	1.17470	1.22993
17	1.40181	1.19062	1.11991	1.24097	1.18692	1.25579	1.22169	1.17845	1.25148	1.17549	1.21962	1.18065	1.23149
18	1.39863	1.19143	1.12003	1.24128	1.17916	1.25473	1.21851	1.17816	1.24284	1.18274	1.22862	1.17825	1.23506
19	1.39583	1.19215	1.12018	1.24105	1.18792	1.25370	1.23000	1.18509	1.24640	1.19295	1.21427	1.18596	1.23802
20	1.39331	1.19280	1.12034	1.24109	1.18776	1.25550	1.22640	1.18039	1.24187	1.21543	1.23527	1.17978	1.23773
21	1.39104	1.19339	1.12050	1.24112	1.18772	1.25599	1.23262	1.18849	1.24157	1.23127	1.21970	1.18175	1.24619
22	1.38897	1.19392	1.12067	1.24124	1.18789	1.25571	1.23630	1.18272	1.24200	1.23463	1.23999	1.17833	1.24066
23	1.38711	1.19441	1.12084	1.24135	1.18808	1.25577	1.23598	1.18931	1.24350	1.25423	1.21108	1.18644	1.24199
24	1.38540	1.19485	1.12101	1.24146	1.18826	1.25581	1.23905	1.18390	1.24864	1.24815	1.22650	1.17750	1.24284
25	1.38384	1.19526	1.12116	1.24157	1.18843	1.25584	1.23516	1.18879	1.24349	1.26176	1.21425	1.18148	1.24192
26	1.38241	1.19563	1.12132	1.24166	1.18859	1.25586	1.23747	1.18763	1.24493	1.25717	1.22254	1.18043	1.24294
27	1.38109	1.19597	1.12147	1.24176	1.18874	1.25587	1.23698	1.18816	1.24499	1.26062	1.22636	1.18296	1.24314
28	1.37992	1.19629	1.12162	1.24184	1.18889	1.25587	1.23733	1.18871	1.24526	1.26327	1.22662	1.18409	1.24347
29	1.37879	1.19659	1.12176	1.24193	1.18903	1.25587	1.23718	1.18879	1.24544	1.26621	1.22732	1.18521	1.24376
30	1.37773	1.19686	1.12190	1.24201	1.18916	1.25586	1.23736	1.18906	1.24565	1.26821	1.22974	1.18635	1.24407

are required to obtain effective collision strengths at high temperatures. We used AUTOSTRUCTURE to calculate the infinite-energy Born and dipole line strength limits. Between the last calculated energy point and the two limits, we interpolate taking into account the type of transition in the Burgess–Tully scaled domain (i.e. the quadrature of reduced collision strength over reduced energy Burgess & Tully 1992) to complete the Maxwellian convolution (Eq. (1)).

3. Results

We have obtained R-matrix electron-impact excitation data for the N-like iso-electronic sequence from O II to Zn XXIV (i.e. O^+ and Zn^{23+}). Our effective collision strengths cover five orders of magnitude in temperature $(z+1)^2(2\times10^1,\ 2\times10^6)$ K, where z is the ionic charge (e.g. $z=7$ for Si VIII).

The effective collision strength data will be archived according to the Atomic Data and Analysis Structure (ADAS) data class *adf04* and will be available in OPEN-ADAS and our UK-APAP website[4]. These data can be used to improve the atomic database of astrophysical plasma codes, such as CHIANTI (Dere et al. 1997, 2019) and SPEX (Kaastra et al. 1996, 2020), where no data or less accurate data were available. The ordinary collision strength data will also be archived in OPEN-ADAS[5].

4. Discussion

We selected six ions Fe XX, Ca XIV, Ar XII, S X, Si VIII, and O II across the iso-electronic sequence to assess the quality of our structure and collision calculations.

We first compare the energy levels and transition strengths $\log(gf)$, where g and f are the statistical weight and oscillator strength of the transition, respectively. Figure 1 illustrates the deviation (in percent) of the energy levels in NIST and previous works with respect to the present ones. Generally speaking, the energy levels agree to within ~5% for the high-charge ions (e.g. Fe XX and Ar XII). A larger deviation ($\lesssim$15%) is found for low-charge ions such as O II, in particular, for some of the low-lying energy levels.

Figure 2 shows the deviation of transition strengths $\Delta\log(gf)$ in archival databases and previous works with respect to the present work. We limit the comparison to relatively strong transitions with $\log(gf)\gtrsim10^{-6}$ from the lowest five energy levels of the ground configuration: $2s^22p^3$ ($^4S_{3/2}$,$^2D_{3/2,\ 5/2}$,$^2P_{1/2,\ 3/2}$). Given the relatively low density of astrophysical plasmas, the ionic level population is dominated by the ground and first four metastable levels (Mao et al. 2017). Weak transitions are not expected to significantly impact the astrophysical plasma diagnostics.

Subsequently, we compare the collision data for Fe XX (Sect. 4.1), Ca XIV (Sect. 4.2), Ar XII (Sect. 4.3), S XI (Sect. 4.4), Si VIII (Sect. 4.5), and O II (Sect. 4.6). R-matrix ICFT calculations were performed previously for Fe XX (Witthoeft et al. 2007), Ca XIV (Wang et al. 2018), Ar XII (Ludlow et al. 2010; Wang et al. 2018), S XI (Liang et al. 2011; Wang et al. 2018), and Si VIII (Wang et al. 2018). In addition, calculations were performed previously for Ca XIV with the Dirac atomic R-matrix code (Dong et al. 2012), Si VIII with B-spline R-matrix (Tayal 2012), and O II with B-spline R-matrix (Tayal 2007) and Breit-Pauli R-matrix with pseudo-states (Kisielius et al. 2009).

We use hexbin plots (Carr et al. 1987) to compare the effective collision strengths from the present work with the latest large-scale R-matrix calculations in the literature for Fe XX, Ar XII, and S X. Table 3 provides some statistics of the hexbin plot comparison. Generally speaking, smaller deviations are found at higher temperatures. Since the present work has a significantly larger close-coupling expansion (725 levels), the additional resonances contribute most to the deviation at low and

[4] http://apap-network.org/
[5] http://open.adas.ac.uk/

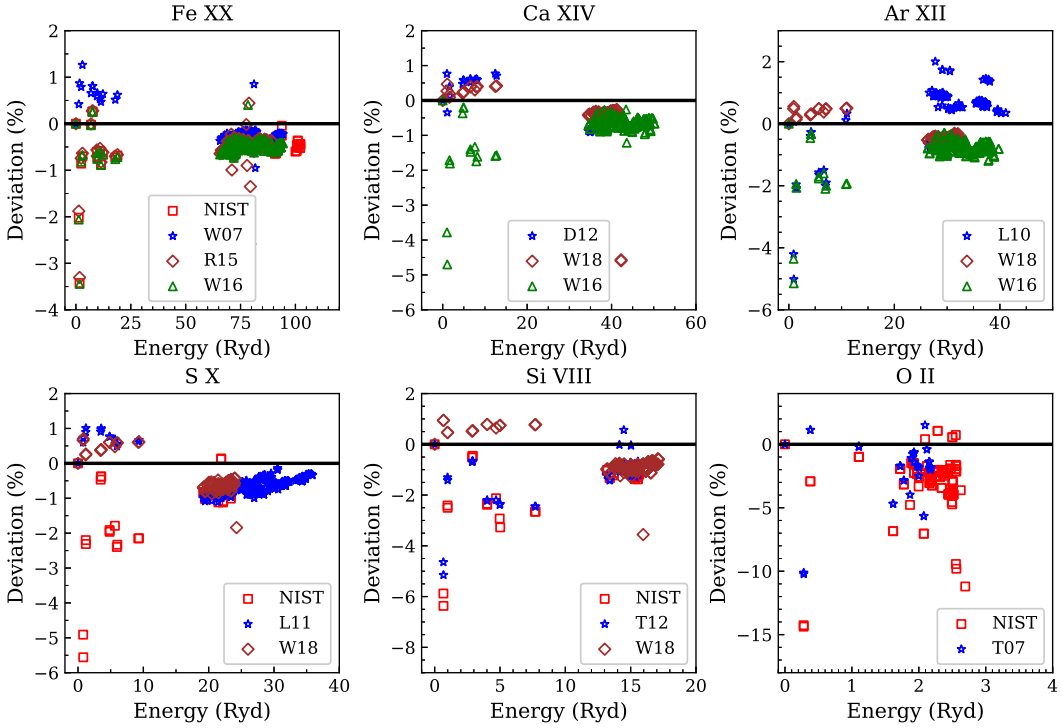

Fig. 1. Percentage deviations between the present energy levels (horizontal lines in black), the experimental ones (NIST) and previous works: W07 refers to Witthoeft et al. (2007), R15 refers to Radžiūtė et al. (2015), W16 refers to Wang et al. (2016), D12 refers to Dong et al. (2012), W18 refers to Wang et al. (2018), L10 refers to Ludlow et al. (2010), L11 refers to Liang et al. (2011), T12 refers to Tayal (2012), and T07 refers to Tayal (2007).

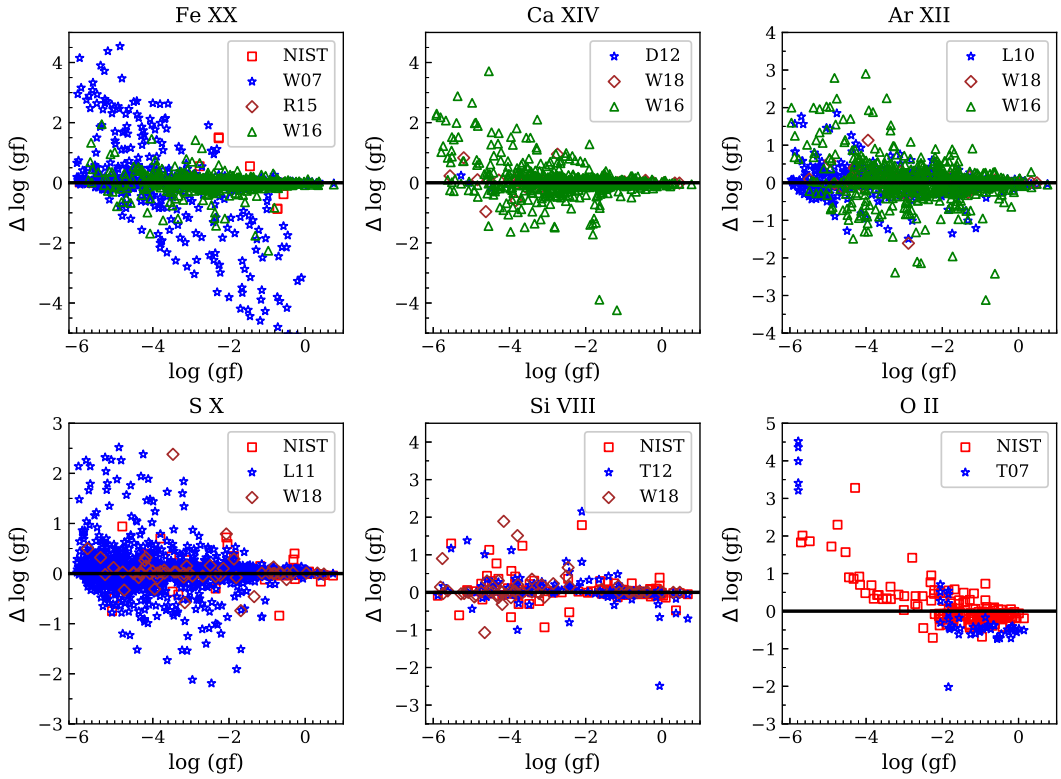

Fig. 2. Comparisons of $\log(gf)$ from the present work (black horizontal line) with the experimental ones (NIST) and previous works: W07 refers to Witthoeft et al. (2007), R15 refers to Radžiūtė et al. (2015), W16 refers to Wang et al. (2016), D12 refers to Dong et al. (2012), W18 refers to Wang et al. (2018), L10 refers to Ludlow et al. (2010), L11 refers to Liang et al. (2011), T12 refers to Tayal (2012), and T07 refers to Tayal (2007). We note that this comparison is limited to relatively strong transitions with $\log(gf) \gtrsim 10^{-6}$ originating from the lowest five energy levels.

Table 3. Statistics of the effective collision strength comparison for Fe XX, Ar XII, and S X.

Ion	T(low)	T(middle)	T(high)	T(low)	T(middle)	T(high)
Fe XX	~41 000 (57%)	~38 000 (58%)	~35 000 (32%)	1480 (23%)	1474 (27%)	1398 (8%)
Ar XII	~12 000 (63%)	~15 000 (57%)	~15 000 (46%)	771 (44%)	889 (29%)	888 (23%)
S X	3438 (80%)	3375 (74%)	3222 (53%)	405 (43%)	402 (33%)	394 (17%)

Notes. Columns #2–#4 give the number of transitions with $\log(\Upsilon) > -5$ in both data sets and the percentage of transitions with deviation larger than 0.2 dex at three temperatures (ion-dependent) used for the hexbin plots. Columns #5–#7 are the statistics when limiting the transitions from the lowest five transitions (i.e. the ground and the first metastable levels).

intermediate temperatures. Similar behaviour was noted also by Fernández-Menchero et al. (2016).

When limiting the comparison to transitions from the lowest five energy levels (i.e. the ground and first four metastable levels), smaller deviations are found at all temperatures. R-matrix calculations without pseudo-states (including the present work) are not converged for the high-lying levels, both with respect to the N-electron target configuration interaction expansion and the $(N + 1)$-electron close-coupling expansion. Therefore, the effective collision strengths obtained in the present and previous works involving high-lying energy levels are not converged. To improve the accuracy of transitions involving the high-lying levels with $n \geq 4$, especially between these high-lying levels, larger-scale R-matrix ICFT calculations or R-matrix calculations with pseudo-state calculations are required.

For Fe XX, Ca XIV, Ar XII, S X, Si VIII, and O II, we also compare selected prominent allowed and forbidden transitions (Table 4) from the ground and metastable levels. Most of these transitions are used to measure the density of the solar atmosphere (Mohan et al. 2003; Del Zanna & Mason 2018). In many cases, effective collision strengths for these density diagnostic lines agree well between the present and previous works.

4.1. Fe XX

The most recent calculation of R-matrix electron-impact excitation data for Fe XX (or Fe^{19+}) is presented by Witthoeft et al. (2007, W07 hereafter). We limit our comparison to W07 and refer readers to W07 for their comparison with other earlier calculations (Butler & Zeippen 2001; McLaughlin & Kirby 2001).

Both W07 and the present work use the AUTOSTRUCTURE code for the structure calculation. As shown in the top-left panel of Fig. 1, the energy levels of the present work and W07 agree within $\lesssim$1%. The first few levels of the present work and W07 differ up to ~4% with respect to NIST, Radžiūtė et al. (2015, R15), and Wang et al. (2016, W16). The latter two more accurate structure calculations were performed with the multi-configuration Dirac-Fock theory and many-body perturbation theory, respectively. As shown in the top-left panel of Fig. 2, the transition strengths agree well between NIST, R15, W16, and the present work with merely a few exceptions. Larger deviations are found between W07 and other works.

Both W07 and the present work use the R-matrix ICFT method for the scattering calculation. W07 included 302 fine-structure levels in the close-coupling expansions. The present work has 725 levels. Figure 3 shows the hexbin plot comparison of the effective collision strengths at $T \sim 2.00 \times 10^5$ K (left), 4.00×10^6 K (middle), and $\sim 8.00 \times 10^7$ K (right). As shown in Fig. 4, the effective collision strengths for the three selected dipole transitions from the ground (12.83 Å) and metastable (12.98 Å and 13.09 Å) levels agree well between the present work and W07.

Table 4. Selected prominent transitions from the lowest three energy levels for Fe XX, Ca XIV, Ar XII, S X, Si VIII, and O II.

Ion	Lower level	Upper level	λ_0 (Å)
Fe XX	$2s^22p^3$ ($^4S_{3/2}$)	$2s^22p^23d$ ($^4P_{3/2}$)	12.83
	$2s^22p^3$ ($^2D_{3/2}$)	$2s^22p^23d$ ($^2D_{5/2}$)	12.98
	$2s^22p^3$ ($^2D_{5/2}$)	$2s^22p^23d$ ($^2F_{7/2}$)	13.09
Ca XIV	$2s^22p^3$ ($^4S_{3/2}$)	$2s2p^4$ ($^4P_{5/2}$)	193.87
	$2s^22p^3$ ($^2D_{5/2}$)	$2s2p^4$ ($^2D_{5/2}$)	166.96
	$2s^22p^3$ ($^2D_{5/2}$)	$2s2p^4$ ($^2P_{3/2}$)	134.27
	$2s^22p^3$ ($^4S_{3/2}$)	$2s^22p^3$ ($^2D_{3/2}$)	943.59 (f)
	$2s^22p^3$ ($^4S_{3/2}$)	$2s^22p^3$ ($^2D_{5/2}$)	880.40 (f)
Ar XII	$2s^22p^3$ ($^4S_{3/2}$)	$2s2p^4$ ($^2P_{5/2}$)	224.25
	$2s^22p^3$ ($^2D_{5/2}$)	$2s2p^4$ ($^2D_{5/2}$)	193.70
	$2s^22p^3$ ($^2D_{5/2}$)	$2s2p^4$ ($^2P_{3/2}$)	154.42
	$2s^22p^3$ ($^4S_{3/2}$)	$2s^22p^3$ ($^2D_{3/2}$)	1054.69 (f)
	$2s^22p^3$ ($^4S_{3/2}$)	$2s^22p^3$ ($^2D_{5/2}$)	1018.72 (f)
S X	$2s^22p^3$ ($^4S_{3/2}$)	$2s2p^4$ ($^2P_{5/2}$)	264.23
	$2s^22p^3$ ($^2D_{5/2}$)	$2s2p^4$ ($^2D_{5/2}$)	228.69
	$2s^22p^3$ ($^2D_{5/2}$)	$2s2p^4$ ($^2P_{3/2}$)	180.73
	$2s^22p^3$ ($^4S_{3/2}$)	$2s^22p^3$ ($^2D_{3/2}$)	1212.93 (f)
	$2s^22p^3$ ($^4S_{3/2}$)	$2s^22p^3$ ($^2D_{5/2}$)	1196.22 (f)
Si VIII	$2s^22p^3$ ($^4S_{3/2}$)	$2s2p^4$ ($^4P_{5/2}$)	319.84
	$2s^22p^3$ ($^2D_{5/2}$)	$2s2p^4$ ($^2D_{5/2}$)	277.06
	$2s^22p^3$ ($^2D_{3/2}$)	$2s2p^4$ ($^2D_{3/2}$)	276.85
	$2s^22p^3$ ($^2D_{5/2}$)	$2s2p^4$ ($^2P_{3/2}$)	216.92
	$2s^22p^3$ ($^4S_{3/2}$)	$2s^22p^3$ ($^2D_{3/2}$)	1445.73 (f)
	$2s^22p^3$ ($^4S_{3/2}$)	$2s^22p^3$ ($^2D_{5/2}$)	1440.51 (f)
O II	$2s^22p^3$ ($^4S_{3/2}$)	$2s^22p^3$ ($^2D_{5/2}$)	3729.88 (f)
	$2s^22p^3$ ($^4S_{3/2}$)	$2s^22p^3$ ($^2D_{3/2}$)	3727.09 (f)
	$2s^22p^3$ ($^4S_{3/2}$)	$2s^22p^3$ ($^2P_{1/2}$)	2470.97 (f)
	$2s^22p^3$ ($^4S_{3/2}$)	$2s^22p^3$ ($^2P_{3/2}$)	2471.09 (f)
	$2s^22p^3$ ($^2D_{5/2}$)	$2s^22p^3$ ($^2P_{1/2}$)	7320.94 (f)
	$2s^22p^3$ ($^2D_{5/2}$)	$2s^22p^3$ ($^2P_{3/2}$)	7322.01 (f)
	$2s^22p^3$ ($^2D_{3/2}$)	$2s^22p^3$ ($^2P_{1/2}$)	7331.69 (f)
	$2s^22p^3$ ($^2D_{3/2}$)	$2s^22p^3$ ($^2P_{3/2}$)	7332.76 (f)

Notes. The rest-frame wavelengths (Å) are taken from the CHIANTI atomic database. Forbidden transitions are labelled with (f).

4.2. Ca XIV

The most recent R-matrix calculations of the electron-impact excitation data of Ca XIV (or Ca^{13+}) are presented in Wang et al. (2018, W18) and Dong et al. (2012, D12 hereafter). The general-purpose relativistic atomic structure package (GRASP) and AUTOSTRUCTURE were used by D12 and W18, respectively, for their atomic structure calculations. The energy levels and transition strengths of D12, W18, and the present work agree well with each other (the upper-middle panels of Fig. 1 and 2).

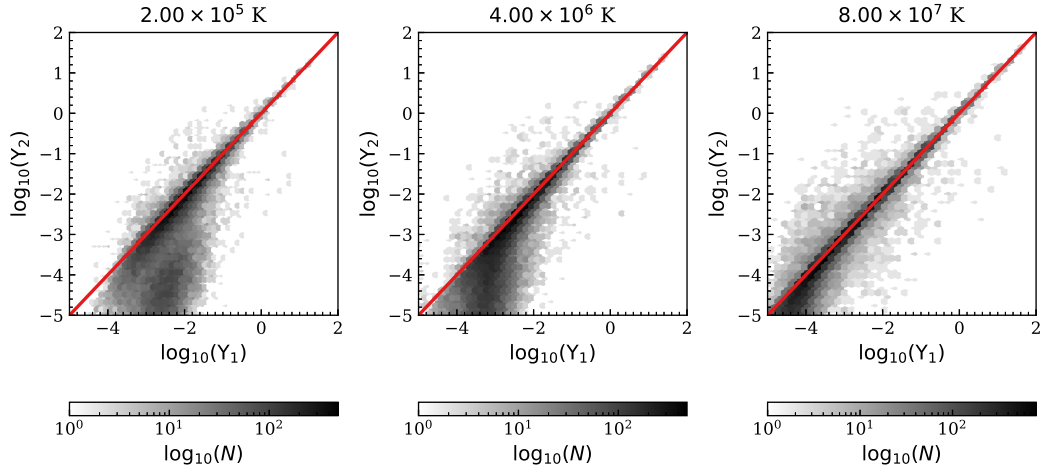

Fig. 3. Hexbin plots of the comparison of the Fe XX (or Fe^{20+}) effective collision strengths between the present work (Υ_1) and Witthoeft et al. (2007, Υ_2) at $T \sim 2.00 \times 10^5$ K (*left*) and 4.00×10^6 K (*middle*), and $\sim 8.00 \times 10^7$ K (*right*). The darker the color is, the greater the number of transitions $\log_{10}(N)$. The diagonal line in red indicates $\Upsilon_1 = \Upsilon_2$.

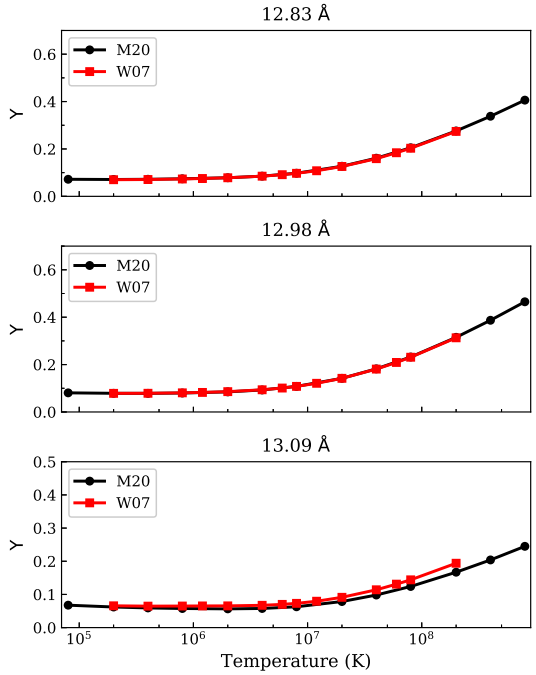

Fig. 4. Comparison of Fe XX (or Fe^{19+}) effective collision strengths between the present work (M20) and Witthoeft et al. (2007, W07) for selected dipole transitions from the ground (*upper*) and metastable (*middle and bottom*) levels listed in Table 4.

D12 included 272 fine-structure levels for the target ion. The Dirac atomic *R*-matrix code (DARC) was used for the collision calculation. Effective collision strengths from the ground level to the lowest 15 levels are tabulated in their Table 4 and archived as supplementary data. The CHIANTI atomic database includes a few more effective collision strengths from the metastable levels provided by Dong et al. (2012). W18 also included 272 fine-structure levels for the target ion. Their scattering calculation was performed via the *R*-matrix ICFT method. Effective collision strengths from the ground level to the lowest 120 levels are tabulated in their Table 22 for Ca XIV.

As shown in Fig. 5, the effective collision strengths of three selected dipole transitions from the ground and metastable levels agree well between the three data sets (D12, W18, and the present work) within the common temperature range. For the two metastable transitions (166.96 Å and 134.27 Å), the extrapolation at higher temperatures in the current version of CHIANTI atomic database (v9.0.1) was not carried out self-consistently, hence the deviations. For the forbidden transition (943.59 Å), the effective collision strengths at $T \lesssim 10^6$ K differ by a factor of two between the present work and W18. Good agreement is found for the other forbidden transition 880.40 Å between the present work, D12, and W18.

We note that the two forbidden lines from the $^2D_{5/2,3/2}$ to the ground state for Ca XIV, observed at 880.4 Å and 943.6 Å respectively, are useful density diagnostics, being relatively close in wavelength. These lines have been observed with several solar instruments, most notably the SUMER (Solar Ultraviolet Measurements of Emitted Radiation) spectrograph on SOHO (Solar and Heliospheric Observatory, see e.g. Curdt et al. (2004). Landi et al. (2003) reported SUMER observations of post-flare loops and noted significant discrepancies (factors of up to 10) between the densities obtained from different ions. They used CHIANTI version 3 atomic data, which included DW rates for Ca XIV and Ar XII. For Ca XIV, no density was obtained, as the observed ratio was below the low-density limit, as shown in Fig. 6. To provide an application of the present atomic rates in solar observations, we built a development version of CHIANTI with the present data. We obtain a density of 1.05×10^9 cm^{-3}.

4.3. Ar XII

The most recent *R*-matrix calculations of electron-impact excitation data for Ar XII (or Ar^{11+}) are presented in Wang et al. (2018, W18) and Ludlow et al. (2010, L10 hereafter). L10, W18, and the present work all used AUTOSTRUCTURE for the atomic structure calculation. As shown in the upper-right panel of Fig. 1, the energies of the low-lying levels in L10 agree well with Wang et al. (2016, W16), which was calculated with the many-body perturbation theory. The energies of the high-lying levels in L10 are ~2–3% offset with respect to W16. The level energies of W18 and the present work agree with each other to within ~1%, with up to ~5% deviation with respect to W16 for the low-lying transitions. The transition strengths of L10, W16, W18, and the present work agree well with each other (the upper-right panel of Fig. 2).

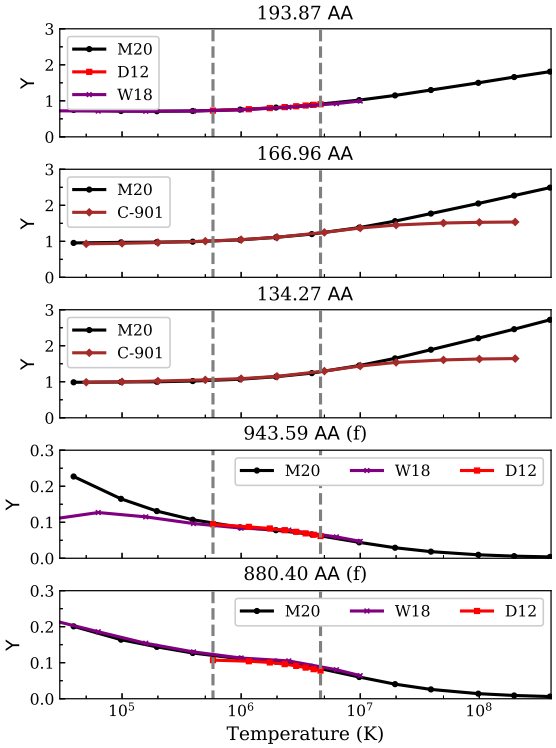

Fig. 5. Comparison of Ca XIV (or Ca^{13+}) effective collision strengths between the present work (M20), Dong et al. (2012, D12), and Wang et al. (2018, W18) for selected transitions listed in Table 4. The *top panel* is a dipole transition from the ground level. For the two dipole metastable transitions (in the second and third panels from the top), effective collision strengths C-901 are obtained directly from the CHIANTI atomic database. The vertical dashed lines indicate the temperature range originally provided by Dong et al. (2012). The brown diamonds outside this temperature range are extrapolated data in CHIANTI. The bottom two panels are forbidden transitions from the ground level to the first two metastable levels.

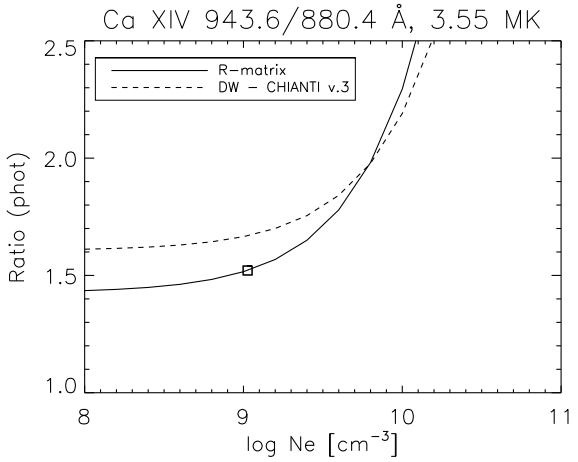

Fig. 6. Line ratios (in phot cm^{-2} s^{-1}) for key diagnostics lines of Ca XIV as a function of density at a fixed temperature of 3.55×10^6 K (the peak ion abundance in ionisation equilibrium). The solid curve is calculated with the present *R*-matrix data, while the dashed curve use distorted wave data as incorporated in CHIANTI version 3. The square indicates the measurement from a post-flare solar SUMER observation (Landi et al. 2003).

L10, W18 and the present work all used the *R*-matrix ICFT method for the scattering calculation. L10 included 186 fine-structure levels of the target ion. At the low temperature end (2.88×10^4–2.88×10^5 K), effective collision strengths for transitions involving levels #158 to #186 might have some issues in their post-processing of the ordinary collision strengths (see Appendix A). W18 included 272 fine-structure levels of the target ion. Effective collision strengths from the ground level to the lowest 120 levels are tabulated in their Table 28 for Ar XII. Figure 7 shows the hexbin plot comparison of the effective collision strengths at $T \sim 1.44 \times 10^5$ K (left) and 2.88×10^6 K (middle), and $\sim 1.44 \times 10^7$ K (right).

As shown in Fig. 8, the effective collision strengths of three selected dipole transitions from the ground and metastable levels agree well between the four data sets: present work (M20), Ludlow et al. (2010, L10), Wang et al. (2018, W18) and Eissner et al. (2005, distorted wave) as incorporated in the CHIANTI atomic database v9.0.1 (C-901). For the forbidden transitions from the ground to the first two metastable levels (1054.69 Å and 1018.72 Å), while the three *R*-matrix data sets agree better with each other, the distorted wave (DW) data set (Eissner et al. 2005) as incorporated in the CHIANTI atomic database v9.0.1 differs by a factor of two at $T \lesssim 10^7$ K.

As for Ca XIV, we built a development version of CHIANTI with the present data of Ar XII. The radiative data in the public version v9.0.1 originated from Eissner et al. (2005). In the development version, we use the A-values (i.e. transition probabilities) of the present work with the exception of the transition $2s^2 2p^3(^2D_{5/2})$ to $2s^2 2p^3(^2D_{3/2})$, as the A-value of this transition in the present work is 0.77, a factor of ~2 larger than that of a multi-configuration Dirac-Fock calculation from C. Froese Fischer[6] and Eissner et al. (2005). The rest of the A-values agree with these two sources to within 20%.

Within the $2s^2 2p^3$ ground configuration, the two forbidden transitions at 1018.72 Å and 1054.69 Å (Table 4) are the most important plasma diagnostics lines. These two UV lines have been observed by several solar instruments, most notably with SOHO/SUMER). They are potentially very useful to measure the solar Ar abundance. Due to the lack of photospheric lines, the solar Ar abundance cannot be measured directly (Lodders 2008). It can be derived indirectly from solar wind measurements by comparing line intensities of Ar with those from other elements. According to Fig. 8, we expect large difference in the line ratios of the development and public versions of CHIANTI. The top panel of Fig. 9 shows the line ratio between the forbidden transition at 1054.69 Å (the stronger of the two) and the resonance transition at 224.2 Å (Table 4). As the resonance transition is mainly populated by direct excitation from the ground level via a strong dipole allowed transition, large differences between the distorted wave and the *R*-matrix ratios are not seen (Fig. 8). On the other hand, the increase in the effective collision strength (Fig. 8) leads to the increase of nearly a factor of two in the line ratio.

The two forbidden lines are also very useful to measure electron densities in active regions, as they are close in wavelength. The lower panel of Fig. 9 shows the line ratio between the two forbidden transitions as a function of density at a fixed temperature of 2.5×10^6 K (the peak of ion abundance in ionisation equilibrium). It is clear that significant differences in the theoretical ratio are present at higher densities, typical of active regions and flares. We also show the measurement by Landi et al. (2003) from SUMER observations of active region post-flare loops. The

[6] https://nlte.nist.gov/MCHF/Elements/Ar/N_18.32.mcdhfSD-lin.dat.mp

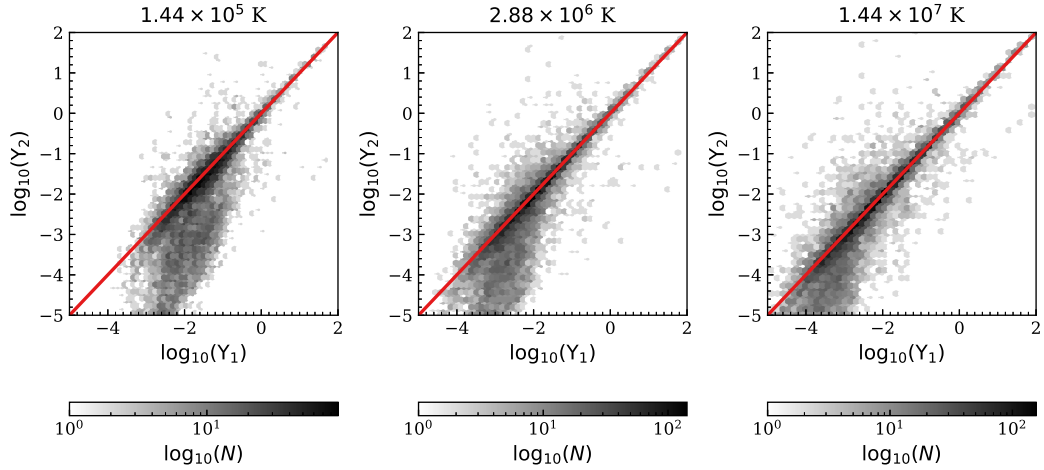

Fig. 7. Hexbin plots of the comparison of the Ar XII (or Ar^{11+}) effective collision strengths between the present work (Υ_1) and Ludlow et al. (2010, Υ_2) at $T \sim 1.44 \times 10^5$ K (*left*) and 2.88×10^6 K (*middle*), and $\sim 1.44 \times 10^7$ K (*right*). The darker the color is, the greater the number of transitions $\log_{10}(N)$. The diagonal line in red indicates $\Upsilon_1 = \Upsilon_2$.

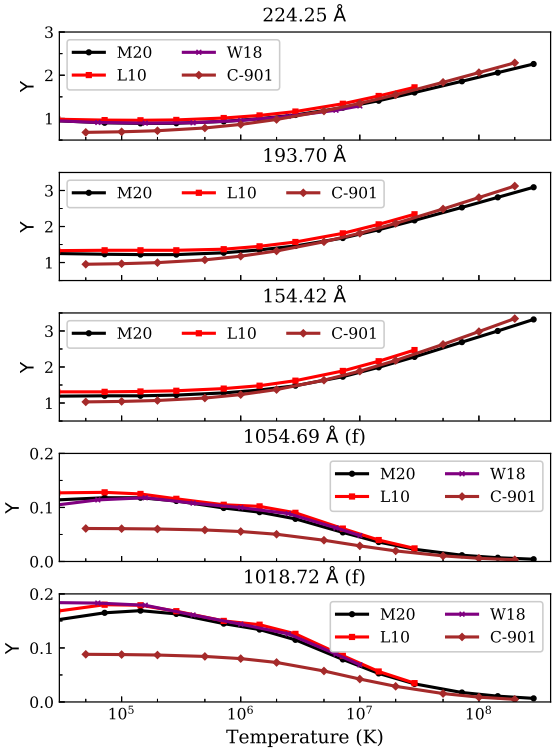

Fig. 8. Comparison of Ar XII (or Ar^{11+}) effective collision strengths between the present work (M20), Ludlow et al. (2010, L10), Wang et al. (2018, W18) and Eissner et al. (2005, distorted wave) as incorporated in the CHIANTI atomic database v9.0.1 (C-901) for selected transitions listed in Table 4. The *top panel* is a dipole transition from the ground level, followed by two metastable transitions. The *bottom two panels* are forbidden transitions from the ground level to the first two metastable levels.

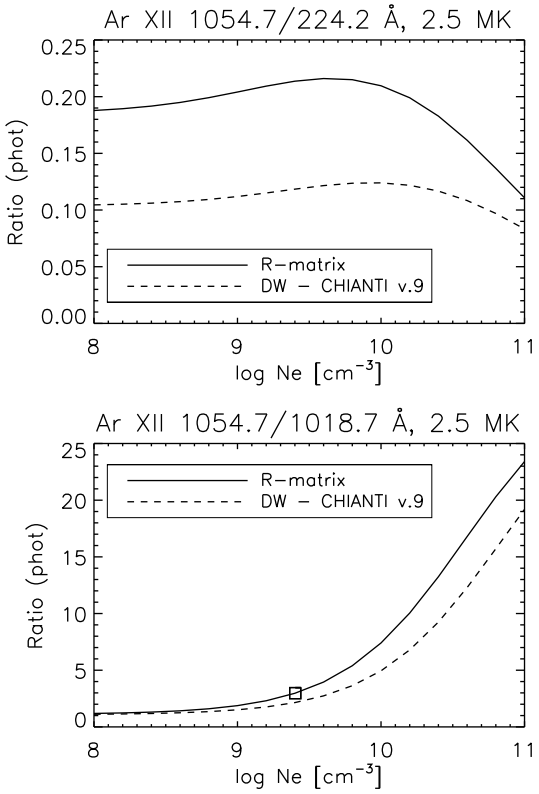

Fig. 9. Line ratios (in phot cm^{-2} s^{-1}) for key diagnostic lines of Ar XII as a function of density at a fixed temperature of 2.5×10^6 K. The solid curve is calculated with the present *R*-matrix data, while the dashed curve used the distorted wave data of Eissner et al. (2005), as incorporated in CHIANTI v9.0.1. The *upper panel* is the line ratio between the forbidden transition at 1054.7 Å and the resonance transition at 224.2 Å, while the *lower panel* is the line ratio between two forbidden transitions (Table 4). The measurement (square) in the *lower panel* is from a post-flare solar SUMER observation (Landi et al. 2003).

two lines were observed within 5 min. The derived density we obtain is 2.9×10^9 cm^{-3}, nearly a factor of two lower than that obtained with the DW data, and in good agreement with the density we have obtained from the Ca XIV lines, considering the different formation temperature of the two ions.

Two other strong forbidden transitions within the ground configuration have also been observed in the EUV by SUMER (Curdt et al. 2004). They are the decays to the ground state from the $^2P_{3/2,1/2}$ levels, at 649.1 Å and 670.3 Å, respectively. They are in principle also useful density diagnostics, as they are close in wavelength. However, the 649.1 Å line is blended with a Si

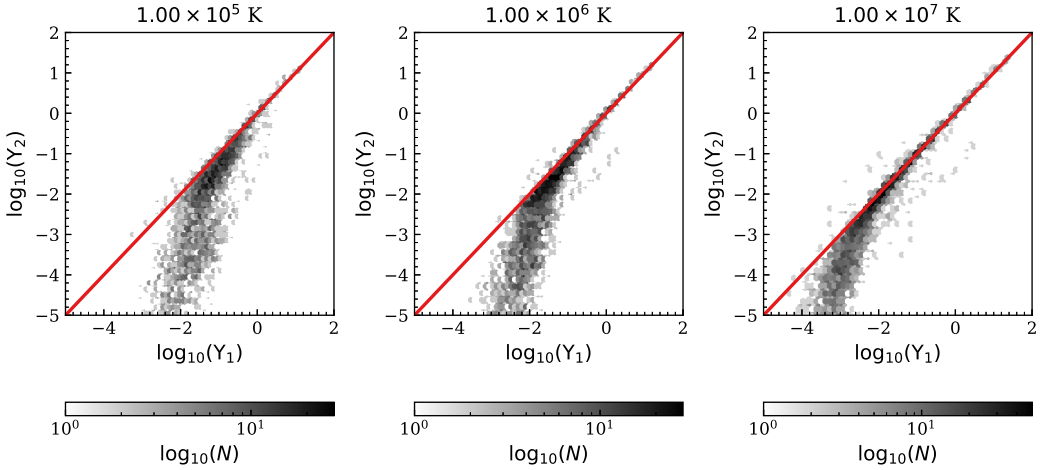

Fig. 10. Hexbin plots of the comparison of the S X (or S^{9+}) effective collision strengths between the present work (Υ_1) and Liang et al. (2011, Υ_2) at $T \sim 1.00 \times 10^5$ K (*left*) and 1.00×10^6 K (*middle*), and $\sim 1.00 \times 10^7$ K (*right*). The darker the color is, the greater the number of transitions $\log_{10}(N)$. The diagonal line in red indicates $\Upsilon_1 = \Upsilon_2$.

X transition. These lines were observed one hour apart from the 1018.7, 1054.7 Å lines (Landi et al. 2003), hence their intensities cannot be directly compared.

4.4. S X

The most recent *R*-matrix calculations of electron-impact excitation data for S X (or S^{9+}) are presented in Wang et al. (2018, W18) and Liang et al. (2011, L11 hereafter).

L11, W18 and the present work all used AUTOSTRUCTURE for the atomic structure calculation. As shown in the bottom-left panel of Fig. 1, the level energies of L11, W18, and the present work agree with each other within ∼1−2% with up to ∼6−7% deviation with respect to NIST for the low-lying transitions. The transition strengths of NIST, L11, W18, and the present work agree well with each other (the bottom-left panel of Fig. 2).

L11, W18 and the present work all used the *R*-matrix ICFT method for the scattering calculation. L11 included 84 fine-structure levels of their effective collision strengths. W18 included 272 fine-structure levels of the target ion. Effective collision strengths from the ground level to the lowest 120 levels are tabulated in their Table 26 for S X. Figure 10 shows the hexbin plot comparison of the effective collision strengths at $T \sim 1.00 \times 10^5$ K (left) and 1.00×10^6 K (middle), and $\sim 1.00 \times 10^7$ K (right).

As shown in Fig. 11, the effective collision strengths of three selected dipole transitions from the ground and metastable levels agree well between the four data sets: present work (M20), Liang et al. (2011, L11), Wang et al. (2018, W18), and Bell & Ramsbottom (2000, *R*-matrix) as incorporated in the CHIANTI atomic database v9.0.1 (C-901). For the two forbidden transitions from the ground to the first two metastable levels (1212.93 Å and 1196.22 Å), at $T \lesssim 10^6$ K, the present work agrees with W18, while L11 is larger by a factor of two and C-901 is smaller by a factor of two. At $T \gtrsim 10^7$ K, the present work agrees with L11, while C-901 is larger by an order of magnitude.

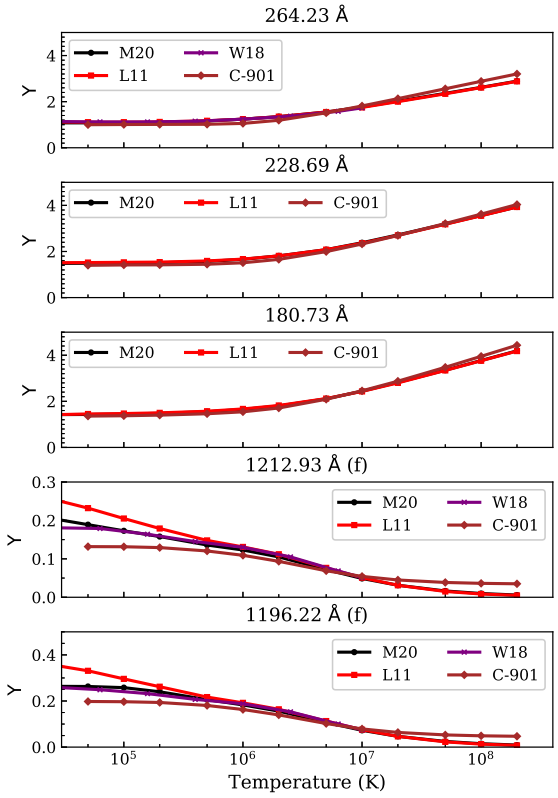

Fig. 11. Comparison of S X (or S^{9+}) effective collision strengths between the present work (M20), Liang et al. (2011, L11), Wang et al. (2018, W18) and Bell & Ramsbottom (2000, *R*-matrix) as incorporated in the CHIANTI atomic database v9.0.1 (C-901) for selected transitions listed in Table 4. The *top panel* is a dipole transition from the ground level, followed by two metastable transitions. The *bottom two panels* are forbidden transitions from the ground level to the first two metastable levels.

4.5. Si VIII

The most recent *R*-matrix calculations of electron-impact excitation data for Si VIII (or Si^{7+}) are presented in Wang et al. (2018, W18) and Tayal (2012, T12).

Both W18 and the present work used AUTOSTRUCTURE for the atomic structure calculation, while T12 used the multi-configuration Hartree-Fock method. As shown in the bottom-middle panel of Fig. 1, the level energies of W18 and the present work agree with each other within ∼1−2% with up to ∼8%

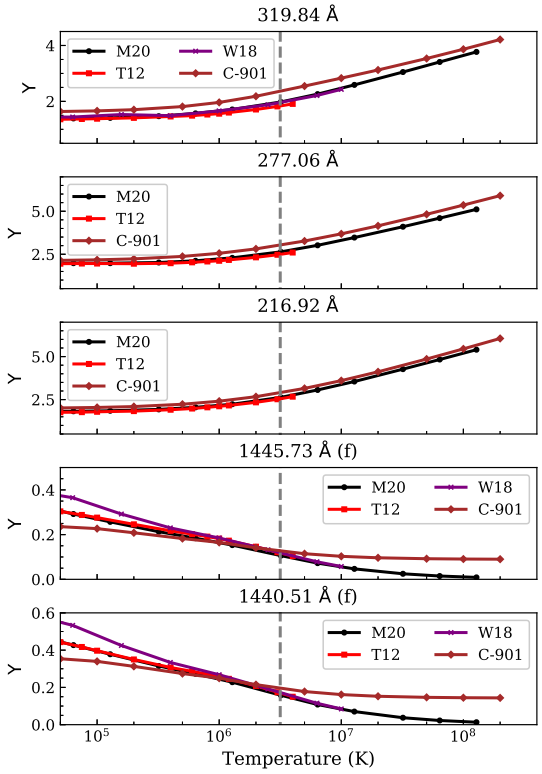

Fig. 12. Comparison of Si VIII (or Si^{7+}) effective collision strengths between the present work (M20), Tayal (2012, T12), Wang et al. (2018, W18), and Bell et al. (2001) as incorporated in the CHIANTI atomic database v9.0.1 (C-901) for selected transitions listed in Table 4. The *top panel* is a dipole transition from the ground level, followed by two metastable transitions. The *bottom two panels* are forbidden transitions from the ground level to the first two metastable levels. The vertical dashed lines indicate the upper temperature limit originally provided by Bell et al. (2001). The brown diamonds beyond this temperature limit are extrapolated in CHIANTI.

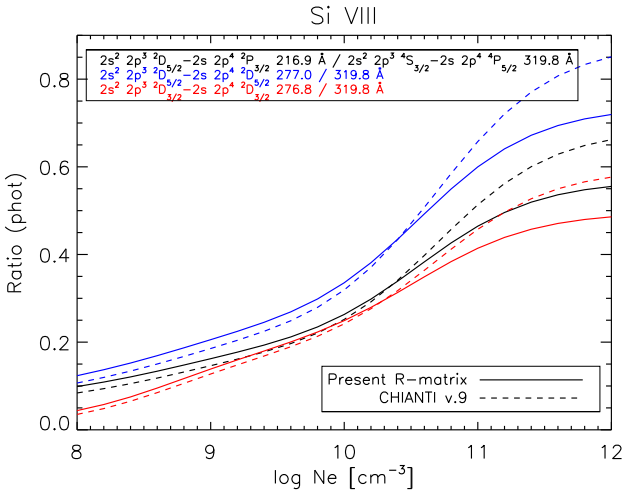

Fig. 13. Line ratios (in phot cm^{-2} s^{-1}) of selected resonance lines (Table 4) of Si VIII as a function of density. The solid curves are calculated with the present *R*-matrix data, while the dashed curves use the *R*-matrix data of Bell et al. (2001) as incorporated in CHIANTI v9.0.1.

deviation with respect to NIST and T12 for the low-lying transitions. The transition strengths of NIST, T12, W18, and the present work agree well with each other (the bottom-middle panel of Fig. 2).

Both W18 and the present work used the *R*-matrix ICFT method for the scattering calculation, while T12 used the B-spline *R*-matrix method. T12 included 68 fine-structure target levels for their effective collision strengths. W18 included 272 fine-structure levels of the target ion. Effective collision strengths from the ground level to the lowest 120 levels are tabulated in their Table 26 for Si VIII.

In Fig. 12, we compare the effective collision strengths of selected transitions listed in Table 4. The values for the three dipole transitions from the ground and metastable levels agree well between the three data sets: present work (M20), Tayal (2012, T12), Wang et al. (2018, W18). The *R*-matrix data set of Bell et al. (2001) as incorporated in the CHIANTI atomic database v9.0.1 (C-901) is also comparable to the other *R*-matrix data sets. For the two forbidden transitions from the ground to the first two metastable levels (1445.73 Å and 1440.51 Å), the present work and T12 agree better with each other. The previous *R*-matrix results of Bell et al. (2001) and Wang et al. (2018) are smaller and larger at $T \lesssim 10^{6.5}$ K, respectively. Originally, the data of Bell et al. (2001) are provided in the temperature range of $10^{3.3-6.5}$ K. The extrapolated data of Bell et al. (2001) in the CHIANTI atomic database v9.0.1 is larger than the other *R*-matrix data at $T \lesssim 10^{6.5}$ K.

As in the case of Ar XII, we built a development version of CHIANTI with the present data of Si VIII. In the development version, we use the A-values of the present work with the exception of transitions between the $2s^22p^3$ and $2s2p^4$ configurations, where values from a multi-configuration Hartree-Fock calculation by Tachiev & Froese Fischer (2002) were used. In the public version of CHIANTI (v9.0.1), the A-values draws from several sources (Merkelis et al. 1999; Zhang & Sampson 1999; Bhatia & Landi 2003). The effective collision strengths use the *R*-matrix data of Bell et al. (2001) for the ground configuration and distorted wave data (Zhang & Sampson 1999; Bhatia & Landi 2003) for the rest.

Within the $2s^22p^3$ ground configuration, the two forbidden transitions at 1440.5 Å and 1445.7 Å (Table 4), are the most important plasma diagnostic lines. As there is little difference between the *R*-matrix data of Bell et al. (2001) and the present work (Fig. 12) at $T \sim 10^6$ K, for solar observations, the electron density derived from the line ratio of the two agree well (~3%). Several other density diagnostic line ratios are also available in the EUV band. Three of them are displayed in Fig. 13. For these lines, some differences between the previous CHIANTI model and the present one are clear, especially at higher densities. A detailed comparison with solar observations is complicated by the fact that the 276.8 Å and 277.0 Å lines are blended with transitions from other ions, and is therefore beyond the scope of this paper.

4.6. O II

The most recent *R*-matrix calculations of electron-impact excitation data for O II (or O^+) are presented in Tayal (2007, T07) and Kisielius et al. (2009, K09).

The present work and T07 used AUTOSTRUCTURE and multi-configuration Hartree-Fock for the atomic structure calculations, respectively. As shown in the bottom-right panel of Fig. 1, the level energies of T07 agree better with respect to NIST than the present work, especially for the low-lying transitions. The transition strengths of NIST, T07, and the present

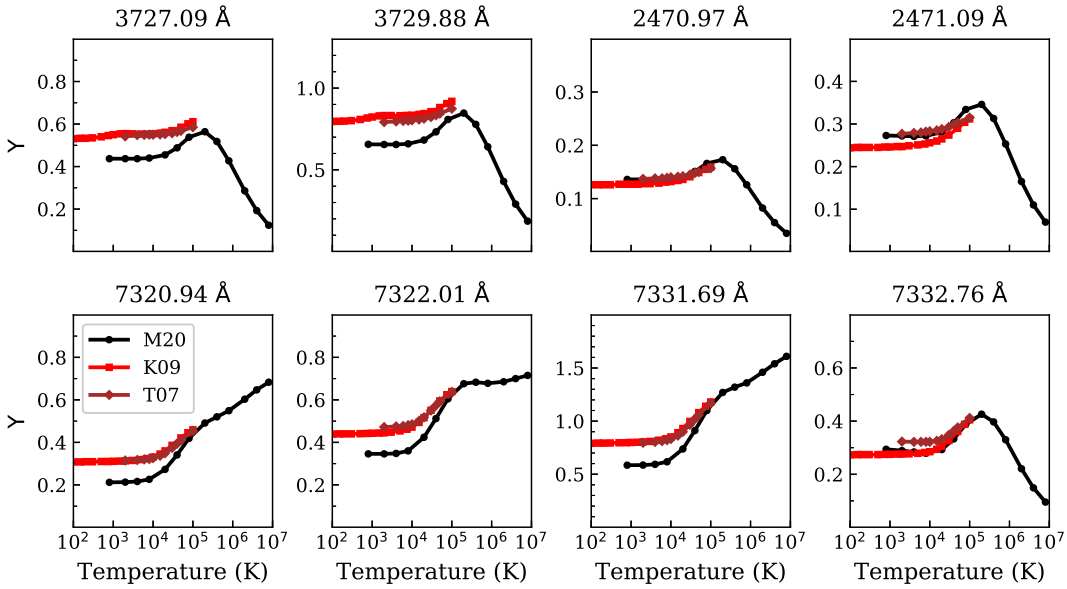

Fig. 14. Comparison of O II (or O^+) effective collision strengths between the present work (M20), Tayal (2007, T07), and Kisielius et al. (2009, K09) for eight common transitions from the ground and metastable levels.

work agree well with each other for $\log(gf) \gtrsim -4$ (the bottom-left panel of Fig. 2).

The present work, T07, and K09 used the *R*-matrix ICFT method, B-spline *R*-matrix method, and Breit–Pauli *R*-matrix method with pseudo-states for the scattering calculations, respectively. T07 provided effective collision strengths for transitions between the lowest 47 energy levels, while K09 focused on transitions between the lowest five energy levels.

In Fig. 14, we compare effective collision strengths of O II (or O^+) between the present work (M20), Tayal (2007, T07), and Kisielius et al. (2009, K09) for eight common transitions from the ground and metastable levels (Table B.1). Both T07 and K09 agree with each other for effective collision strengths at lower temperatures ($T \lesssim 10^5$ K) and, thus, are recommended. We consider our present work less accurate at lower temperatures, mainly due to the poorer atomic structure (Figs. 1 and 2). In general, calculations with non-orthogonal orbitals and pseudo states should be preferred for low-charge ions such as O II, as in our case we are limited by the use of orthogonal orbitals for our *R*-matrix calculations (Sect. 2.1). For transitions not covered by T07 and K09, caution should be exercised when incorporating our data for lower temperatures into atomic databases, for example, as used by photoionisation plasma codes, due to its relatively low accuracy. On the other hand, the present work agrees better with T07 and K09 at $T \gtrsim 10^5$ K. Thus, the effective collision strengths at higher temperatures ($T \gtrsim 10^5$ K), typical of collisional plasmas, can be incorporated freely into the atomic databases of plasma codes.

5. Conclusion

We have presented a systematic set of *R*-matrix intermediate-coupling frame transfer calculations for N-like ions from O II to Zn XXIV (i.e. O^+ to Zn^{23+}) to obtain level-resolved effective collision strengths over a wide temperature range. The extensive comparison made with results in the literature for a sample of ions important for astrophysical applications provides a reassuring picture. Our effective collision strengths from the ground and metastable levels agree, in general, within 0.2 dex with previous state-of-the-art calculations, at temperatures relevant to modelling. Our configuration interaction target and close-coupling collision expansion are significantly larger than previous studies. This indicates that we have reached convergence here. On the other hand, as we have seen in previous studies, collision strengths involving the highest-lying energy levels are not converged.

As accurate *R*-matrix data were available for only some ions, the present calculations are a significant extension and improvement for this iso-electronic sequence. For several minor (cosmicly rare) ions such as Ti XV and Cr XVII, the present data are a significant improvement with respect to previous distorted-wave calculations.

We have shown examples where significant differences are found in the diagnostics (densities, abundances) when compared to CHIANTI models which used only distorted wave data (Ca XIV and Ar XII). Some differences are present also when previous *R*-matrix data are utilised (Si VIII).

The effective collision strengths are archived according to the Atomic Data and Analysis Structure (ADAS) data class *adf04* and will be available in OPEN-ADAS and our UK-APAP website. These data will be incorporated into plasma codes such as CHIANTI (Dere et al. 1997, 2019) and SPEX (Kaastra et al. 1996, 2020). These data can improve the quality of plasma diagnostics especially in the context of future high-resolution spectrometers. We plan to perform similar calculations for the O-like iso-electronic sequence.

Acknowledgements. The present work is funded by STFC (UK) through the University of Strathclyde UK APAP network grant ST/R000743/1 and the University of Cambridge DAMTP atomic astrophysics group grants ST/P000665/1 and ST/T000481/1. We thank Enrico Landi for providing the observed intensities of the SUMER lines. J.M. thanks useful discussions with Helen Mason, Martin O Mullane, and Pete Storey. J.M. acknowledges atomic data provided by G. Jiang. We thank the referee for careful reading of the manuscript and useful suggestions.

References

Badnell, N. R. 2011, Comput. Phys. Commun., 182, 1528
Badnell, N. R., & Griffin, D. C. 2001, J. Phys. B At. Mol. Phys., 34, 681

Badnell, N. R., Del Zanna, G., Fernández-Menchero, L., et al. 2016, J. Phys. B At. Mol. Phys., 49, 094001
Barret, D., Lam Trong, T., den Herder, J.-W., et al. 2018, Proc. SPIE, 106991G
Bell, K. L., & Ramsbottom, C. A. 2000, At. Data Nucl. Data Tables, 76, 176
Bell, K. L., Matthews, A., & Ramsbottom, C. A. 2001, MNRAS, 322, 779
Berrington, K. A., Eissner, W. B., & Norrington, P. H. 1995, Comput. Phys. Commun., 92, 290
Bhatia, A. K., & Landi, E. 2003, At. Data Nucl. Data Tables, 85, 317
Butler, K., & Zeippen, C. J. 2001, A&A, 372, 1078
Burgess, A. 1974, J. Phys. B At. Mol. Phys., 7, L364
Burgess, A., & Tully, J. A. 1992, A&A, 254, 436
Burke, P. G. 2011, R-Matrix Theory of Atomic Collisions: Application to Atomic
Carr, D. B., Littlefield, R. J., Nicholson, W. L., et al. 1987, JASA, 82, 424
Cui, W., Chen, L.-B., Gao, B., et al. 2020, J. Low Temp. Phys., 199, 502
Curdt, W., Landi, E., & Feldman, U. 2004, A&A, 427, 1045
Del Zanna, G., & Mason, H. E. 2018, Liv. Rev. Sol. Phys., 15, 5
Del Zanna, G., Fernández-Menchero, L., & Badnell, N. R. 2019, MNRAS, 484, 4754
Dere, K. P., Landi, E., Mason, H. E., Monsignori Fossi, B. C., & Young, P. R. 1997, A&AS, 125, 149
Dere, K. P., Del Zanna, G., Young, P. R., et al. 2019, ApJS, 241, 22
Dong, F., Wang, F., Zhong, J., et al. 2012, PASJ, 64, 131
Eissner, W., Jones, M., & Nussbaumer, H. 1974, Comput. Phys. Commun., 8, 270
Eissner, W., Landi, E., & Bhatia, A. K. 2005, At. Data Nucl. Data Tables, 89, 139
Fernández-Menchero, L., Giunta, A. S., Del Zanna, G., & Badnell, N. R. 2016, J. Phys. B At. Mol. Phys., 49, 085203
Kaastra, J. S., Mewe, R., & Nieuwenhuijzen, H. 1996, UV and X-ray Spectroscopy of Astrophysical and Laboratory Plasmas, 411
Kaastra, J. S., Raassen, A. J. J., de Plaa, J., & Gu, L. 2020, https://doi.org/10.5281/zenodo.3939056
Kisielius, R., Storey, P. J., Ferland, G. J., et al. 2009, MNRAS, 397, 903
Landi, E., Feldman, U., Innes, D. E., et al. 2003, ApJ, 582, 506
Liang, G. Y., Badnell, N. R., Zhao, G., et al. 2011, A&A, 533, A87
Lodders, K. 2008, ApJ, 674, 607
Ludlow, J. A., Ballance, C. P., Loch, S. D., et al. 2010, J. Phys. B At. Mol. Phys., 43, 074029
Mao, J. 2020, https://doi.org/10.5281/zenodo.4047076
Mao, J., Kaastra, J. S., Mehdipour, M., et al. 2017, A&A, 607, A100
Mao, J., Badnell, N. R., & Del Zanna, G. 2020, A&A, 634, A7
McLaughlin, B. M., & Kirby, K. P. 2001, J. Phys. B At. Mol. Phys., 34, 2255
Merkelis, G., Martinson, I., Kisielius, R., et al. 1999, Phys. Scr., 59, 122
Mohan, A., Landi, E., & Dwivedi, B. N. 2003, ApJ, 582, 1162
Nussbaumer, H., & Storey, P. J. 1978, A&A, 64, 139
Osterbrock, D. E., & Ferland, G. J. 2006, Astrophysics of Gaseous Nebulae and Active Galactic Nuclei (Sausalito, CA: University Science Books)
Radžiūtė, L., Ekman, J., Jönsson, P., et al. 2015, A&A, 582, A61
Ramsbottom, C. A., & Bell, K. L. 1997, A&AS, 125, 543
Smith, R.K., Abraham, M.H., Allured, R., et al. 2016, Proc. SPIE, 9905, 99054M
Tachiev, G. I., & Froese Fischer, C. 2002, A&A, 385, 716
Tayal, S. S. 2007, ApJS, 171, 331
Tayal, S. S. 2012, A&A, 541, A61
Witthoeft, M.C. 2005, OPEN-ADAS
Witthoeft, M. C., Del Zanna, G., & Badnell, N. R. 2007, A&A, 466, 763
Wang, K., Si, R., Dang, W., et al. 2016, ApJS, 223, 3
Wang, H., Jiang, G., Li, X., et al. 2018, ADNDT, 120, 373
Zhang, H. L., & Sampson, D. H. 1999, At. Data Nucl. Data Tables, 72, 153

Appendix A: Ar XII

Ludlow et al. (2010) performed an ICFT *R*-matrix electron-impact excitation calculation for Ar XII. They included 186 fine-structure levels of the target ion. The effective collision strengths are available over a wide temperature range (between 2.88×10^4 K and 2.88×10^7 K).

For transitions involving levels #158 to #186 (their highest energy level), the effective collision strengths at the lowest temperature (2.88×10^4 K) are either zero or $\gtrsim$5 orders of magnitude smaller than that of the next temperature point (7.20×10^5 K). A similar jump with $\gtrsim$4 orders of magnitude is also found between effective collision strengths at 7.20×10^4 K and 1.44×10^5 K for most of the transitions involving levels #158 to #186.

Appendix B: Mg VI

Table B.1. Selected prominent transitions from the lowest three energy levels for Mg VI. The rest-frame wavelength (Å) are taken from the CHIANTI atomic database.

Lower level	Upper level	λ_0 (Å)
$2s^22p^3$ ($^4S_{3/2}$)	$2s2p^4$ ($^2P_{5/2}$)	403.01
$2s^22p^3$ ($^2D_{5/2}$)	$2s2p^4$ ($^2D_{3/2}$)	349.11
$2s^22p^3$ ($^2D_{5/2}$)	$2s2p^4$ ($^2P_{3/2}$)	270.39
$2s^22p^3$ ($^4S_{3/2}$)	$2s^22p^3$ ($^2D_{3/2}$)	1806.00 (f)
$2s^22p^3$ ($^4S_{3/2}$)	$2s^22p^3$ ($^2D_{5/2}$)	1806.42 (f)

The most recent *R*-matrix calculation of electron-impact excitation data for Mg VI (or Mg^{5+}) is presented by Wang et al. (2018, W18). In addition, a data set provided by Witthoeft (2005, W05) is also available from OPEN-ADAS without an associated publication.

W05, W18 and the present work all used the ICFT *R*-matrix method for the scattering calculation. Both W05 and W18 included 272 fine-structure levels of the target ion. For W18, effective collision strengths from the ground level to the lowest 120 levels are tabulated in their Table 22 for Mg VI. For W05, according to the comments in the adf04 file, the atomic structure is optimised for transitions within $n = 2$ only.

In Fig. B.1, we compare the effective collision strengths of selected three transitions from the ground and metastable levels listed in Table B.1. For the three dipole transitions from the ground and metastable levels, we found good agreement between the three data sets: present work (M20), Witthoeft (2005, W05), and Ramsbottom & Bell (1997, *R*-matrix) as incorporated in the CHIANTI atomic database v9.0.1 (C-901). For the two forbidden transitions from the ground to the first two metastable levels, the extrapolation at higher temperatures in the current version of CHIANTI is inaccurate.

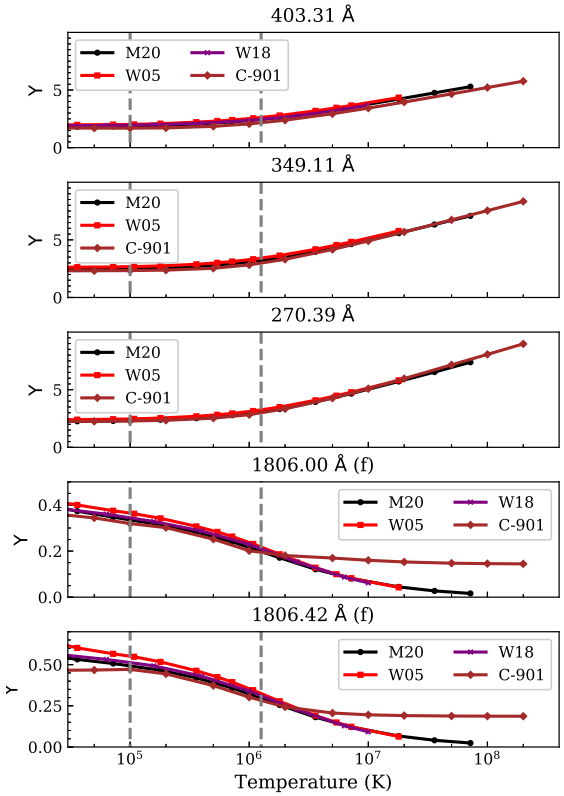

Fig. B.1. Comparison of Mg VI (or Mg^{5+}) effective collision strengths between the present work (M20), Witthoeft (2005, W05), Wang et al. (2018, W18) and Ramsbottom & Bell (1997, *R*-matrix) as incorporated in the CHIANTI atomic database v9.0.1 (C-901) for selected transitions listed in Table B.1. The *top panel* is a dipole transition from the ground level, followed by two metastable transitions. The *bottom two panels* are forbidden transitions from the ground level to the first two metastable levels. The vertical dashed lines indicate the temperature range originally provided by Ramsbottom & Bell (1997). The brown diamonds outside this temperature range is extrapolated in CHIANTI.